The Astrophysical Journal, 629:L45–L48, 2005 August 10

DYNAMIC METEOROLOGY AT THE PHOTOSPHERE OF HD 209458b

Curtis S. Cooper[1] and Adam P. Showman[1]
Received 2005 February 22; accepted 2005 June 28; published 2005 July 18

ABSTRACT

We calculate the meteorology of the close-in transiting extrasolar planet HD 209458b using a global, three-dimensional atmospheric circulation model. Dynamics are driven by perpetual irradiation of one hemisphere of this tidally locked planet. The simulation predicts global temperature contrasts of ~500 K at the photosphere and the development of a steady superrotating jet. The jet extends from the equator to midlatitudes and from the top model layer at 1 mbar down to 10 bar at the base of the heated region. Wind velocities near the equator exceed 4 km s^{-1} at 300 mbar. The hottest regions of the atmosphere are blown downstream from the substellar point by ~60° of longitude. We predict from these results a factor of ~2 ratio between the maximum and minimum observed radiation from the planet over a full orbital period, with peak infrared emission preceding the time of the secondary eclipse by ~14 hr.

Subject headings: atmospheric effects — planets and satellites: general — planets and satellites: individual (HD 209458b) — methods: numerical

1. INTRODUCTION

The transiting planet HD 209458b orbits very closely (0.046 AU) to its parent star with a period of 3.5257 days (Charbonneau et al. 2000; Henry et al. 2000). From transit depth measurements, the mass and radius of HD 209458b are known fairly accurately: $(0.69 \pm 0.05)M_{\rm Jupiter}$ and $(1.32 \pm 0.05)R_{\rm Jupiter}$ (Laughlin et al. 2005). The age of the system is estimated to be 5.2 Gyr, with uncertainties of ~10%. Furthermore, owing to careful measurements of the stellar spectrum during the planet's transit, much is now known about HD 209458b's atmospheric properties (Brown et al. 2001; Charbonneau et al. 2002; Vidal-Madjar et al. 2003, 2004).

Considerable work has been done to model the spectra, physical structure, and time evolution of extrasolar giant planets (EGPs; Burrows et al. 2004; Chabrier et al. 2004; Iro et al. 2005). Relatively less effort, however, has been spent on EGP meteorologies; i.e., global temperature and pressure fluctuations, wind velocities, and cloud properties. Preliminary simulations of the circulation by Showman & Guillot (2002) and the shallow-water calculations of Cho et al. (2003) suggest that close-in systems like HD 209458b—with strong day-night heating contrasts and modest rotation rates—occupy a dynamically interesting regime.

In this Letter, we report on the results from a multilayer global atmospheric dynamics model of HD 209458b. Our results—the existence of a fast superrotating equatorial jet at the photosphere that blows the hottest regions downwind—qualitatively agree with previous three-dimensional numerical simulations by Showman & Guillot (2002). The simulation presented here, however, adopts more realistic radiative-equilibrium temperature profiles and timescales, superior resolution, and a domain that extends deeper into the interior. In particular, the simulations of Showman & Guillot (2002) could not accurately predict the day-night temperature difference at the photosphere. We here predict this temperature difference to be ~500 K, in agreement with order of magnitude estimates by Showman & Guillot (2002).

Our calculations have implications for the planet's infrared (IR) light curve. With the first IR detections of the transiting EGPs TrES-1 and HD 209458b (Charbonneau et al. 2005; Deming et al. 2005), observational constraints on the meteorologies of close-in giant planets will likely be possible over the next 2 years.

[1] Department of Planetary Sciences and Lunar and Planetary Laboratory, University of Arizona, 1629 University Boulevard, Tucson, AZ 85721; curtis@lpl.arizona.edu, showman@lpl.arizona.edu.

2. MODEL

Our model of the general circulation of HD 209458b integrates the primitive equations of dynamical meteorology using version 2 of the ARIES/GEOS Dynamical Core (AGDC2; Suarez & Takacs 1995). The primitive equations filter vertically propagating sound waves but retain horizontally propagating external sound waves (called Lamb waves; Kalnay 2003).

The grid spacing is 5° × 4° in longitude and latitude, respectively (~7000 km near the equator). We use 40 vertical levels spaced evenly in log-pressure between 1 mbar and 3 kbar. This spacing implies that we resolve each pressure scale height with approximately two model layers. The scale height ranges from 500 to 1500 km over the domain of integration.

Following Guillot et al. (1996) and Showman & Guillot (2002), we assume synchronous rotation. The acceleration of gravity, which does not vary significantly over the pressure range considered, is set to $g = 9.42$ m s^{-2}. We take the mean molecular weight and heat capacity to be constant: $c_p = 1.43 \times 10^4$ J kg^{-1} K^{-1} and $\mu = 1.81 \times 10^{-3}$ kg mol^{-1}, which neglects the ~30% variations in these parameters caused by dissociation of molecular hydrogen at the deepest pressures in the model.

The intense stellar irradiation extends the radiative zone of HD 209458b all the way down to ~1 kbar pressure, with a depth ~5%–10% of the planetary radius (Burrows et al. 2003; Chabrier et al. 2004). Our integrations do not solve the equation of radiative transfer directly. Rather, we treat the effects of the strong stellar insolation using a Newtonian radiative scheme in which the thermodynamic heating rate q (W kg^{-1}) is given by

$$\frac{q}{c_p} = -\frac{T(\lambda, \phi, p, t) - T_{\rm eq}(\lambda, \phi, p)}{\tau_{\rm rad}(p)}, \qquad (1)$$

which relaxes the model temperature T toward a prescribed radiative-equilibrium temperature $T_{\rm eq}$. In equation (1), λ, ϕ, p, and t are longitude, latitude, pressure, and time. The radiative-

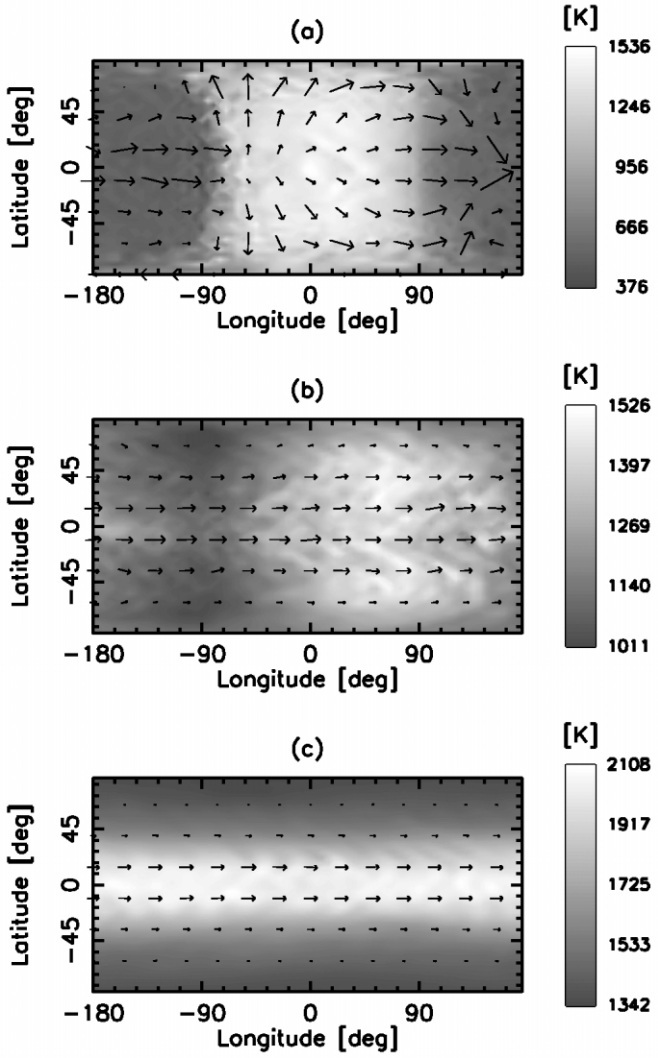

FIG. 1.—Snapshot at 5000 Earth days of simulated temperature (*gray scale*) and winds (*arrows*) on three isobars: (*a*) 2.5 mbar, (*b*) 220 mbar, and (*c*) 19.6 bar. The substellar point is at (0, 0) in longitude and latitude. Peak winds are 9.2, 4.1, and 2.8 km s^{-1} in (*a*), (*b*), and (*c*). The simulated temperature difference of ~500 K at 220 mbar is less than the assumed temperature difference of 920 K in radiative equilibrium due to advection of hot material from the dayside to the nightside by eastward winds of ~4 km s^{-1} on this layer.

equilibrium temperature T_{eq} and the timescale for relaxation to radiative equilibrium τ_{rad} are inputs of the AGDC2.

We rely on the radiative-equilibrium calculations of Iro et al. (2005) to specify $T_{eq}(\lambda, \phi, p)$ and $\tau_{rad}(p)$. Iro et al. (2005) use the multiwavelength atmosphere code of Goukenleuque et al. (2000) to calculate the radiative-equilibrium temperature structure of HD 209458b for a single vertical column, hereafter denoted as $T_{Iro}(p)$. Iro et al. (2005) assume globally averaged insolation conditions (i.e., they redistribute the incident solar flux over the entire globe). Their calculation includes the opacities appropriate for a solar-abundance distribution of gas (Anders & Grevesse 1989), including the neutral alkali metals Na and K.

Iro et al. (2005) do not consider condensation or the scattering and absorption of radiation by silicate clouds, which can conceivably form near the photosphere (see, e.g., Fortney et al. 2003). Condensates can potentially have a significant effect on the planet's radiation balance, depending on the depth at which they form, the particle sizes, and the vertical extent of cloud layers (Cooper et al. 2003). The net direction of this effect (i.e., to warm the atmosphere or to cool it) is as yet unclear and remains a subject for future work.

Iro et al. (2005) compute radiative-relaxation timescales as a function of p from 0.01 mbar down to 10 bar by applying a Gaussian perturbation to the radiative-equilibrium temperature profile at each vertical level. We use their radiative-relaxation timescales for $\tau_{rad}(p)$ in equation (1). At pressures exceeding 10 bar, radiative relaxation is negligible compared to the dynamical timescales considered here. We simply assume $q = 0$ on all layers from 10 bar to 3 kbar.

To account for the longitude-latitude dependence of T_{eq} in equation (1), we use a simple prescription. We choose the substellar point to be at $(\lambda, \phi) = (0, 0)$. On the dayside, we set

$$T_{eq}^4(\lambda, \phi, p) = T_{night,\,eq}^4(p) + [T_{ss,\,eq}^4(p) - T_{night,\,eq}^4(p)] \cos\lambda \cos\phi, \quad (2)$$

where $T_{ss,\,eq}(p)$ and $T_{night,\,eq}(p)$ are the radiative-equilibrium temperature profiles of the substellar point and nightside (assumed to be uniform over the dark hemisphere), respectively. Equation (2) implies that the hottest T_{eq} profile is at the substellar point. On the nightside, we set $T_{eq}(\lambda, \phi, p)$ equal to $T_{night,\,eq}(p)$.

We treat the radiative-equilibrium temperature difference between the substellar point and the nightside, $\Delta T_{eq}(p) = T_{ss,\,eq}(p) - T_{night,\,eq}(p)$, as a free parameter that is a specified function of pressure. To determine $T_{ss,\,eq}(p)$ and $T_{night,\,eq}(p)$ from the Iro et al. (2005) profile and our specified ΔT_{eq}, we horizontally average T_{eq}^4 on the top layer of our model over the sphere and set it equal to T_{Iro}^4 at that pressure. Based on the ~1000 K day-night temperature differences from Iro et al. (2005), we use $\Delta T_{eq} = 1000$ K for pressures less than 100 mbar and decrease it logarithmically with pressure down to 530 K at the base of the heated region (10 bar). Newtonian cooling is a crude approximation to the true radiative transfer, but the scheme is computationally fast—hence allowing extensive explorations of parameter space—and gives us direct control over the model's diabatic heating.

The model's initial temperature was set to $T_{night,\,eq}(p)$ everywhere over the globe; there were no initial winds. We set the time step equal to 50 s, which is much smaller than the time step required for numerical stability according to the Courant-Friedrichs-Lewy criterion (Kalnay 2003).

3. RESULTS AND DISCUSSION

By 5000 days of simulation time, the simulation has reached a statistical steady state, at least down to the 3 bar level, which is the level above which 99% of the stellar photons are absorbed (Iro et al. 2005). Deeper than 3 bar, the kinetic energy continues to increase with time as these layers respond to the intense irradiation on relatively long timescales $\tau_{rad} \sim 1$ yr.

At pressures less than 10 bar, the model rapidly develops strong winds and temperature variability in response to the imposed day-night heating contrast. The upper atmosphere is nearly in radiative equilibrium (Fig. 1*a*), with temperature contrasts of ~1000 K. This results from the fact that the radiative-equilibrium time constant τ_{rad} at 2 mbar is only ~1 hr, which is much shorter than the timescale for winds to advect heat across a hemisphere.

At 2 mbar pressures, supersonic winds exceeding 9 km s^{-1} appear at high latitudes, with strong north-south as well as east-west flow. Supersonic winds are plausible in the dynamical

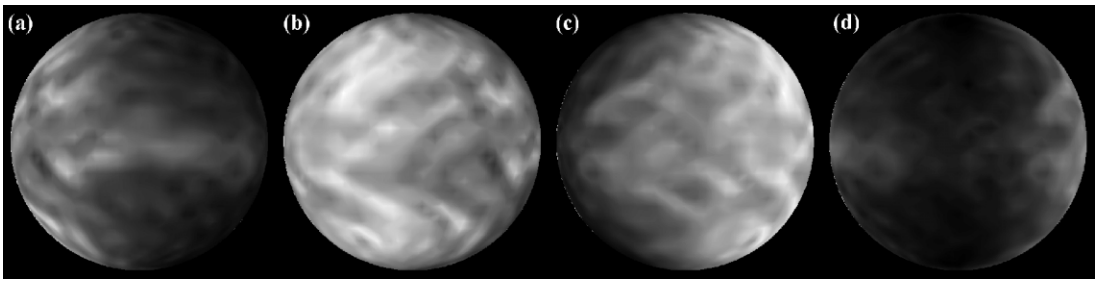

FIG. 2.—Flux from HD 209458b as it would appear from Earth at four orbital phases: (*a*) in transit, (*b*) one-quarter after the transit, (*c*) in secondary eclipse, and (*d*) one-quarter before the next transit. The planetary rotation axes are vertical, with the superrotating jet seen in Fig. 1 going from left to right in each panel. The temperature on this layer ranges from 1011 K (*dark*) to 1526 K (*bright*). In radiative equilibrium, panel *a* would be darkest and *c* would be brightest. The globes show that a difference in observed flux from the planet between the leading and trailing phases of its orbit—panels *b* and *d*—is a signature of winds.

regime of HD 209458b due to the immense radiative forcing from the parent star. For comparison, the planet Neptune has high-velocity zonal jets with wind speeds approaching the local speed of sound (Limaye & Sromovsky 1991), but the radiative forcing is a million times weaker than it is for HD 209458b.

In contrast, the flow near the photosphere near 220 mbar is dominated by an eastward jet extending from the equator to midlatitudes (Fig. 1*b*). The temperature contrasts reach ~500 K at this level, with the hottest part of the atmosphere advected ~60° downstream from the substellar point by the 4 km s^{-1} eastward jet. Here the time constant for relaxation to the radiative equilibrium τ_{rad} is several Earth days. The downstream advection of the hottest regions results from the fact that the radiative and advection timescales are comparable at this level. The small-scale barlike features visible in Figure 1*b* propagate nearly horizontally westward relative to the flow at ~3 km s^{-1}, which is close to the speed of sound. These features are most consistent with Lamb waves (Kalnay 2003, p. 42).

At 19.6 bar, the equatorial winds remain extremely fast—2.8 km s^{-1}—but the temperature structure exhibits little longitudinal variability (Fig. 1*c*). Our model's circulation results entirely from radiative heating occurring at pressures less than 10 bar. Therefore, any winds or temperature variability that develops at pressures exceeding 10 bar results solely from downward transport of energy from the overlying heated layers by vertical advection or wave transport. The layers between 3 and 30 bar contain ~70% of the atmosphere's kinetic energy. Lower pressures have fast winds but little mass, while the winds drop rapidly to zero at pressures exceeding ~30 bar.

The essential assumption of the primitive equations is hydrostatic balance (Holton 1992; Kalnay 2003), an approximation generally valid for shallow flow. This applies to the case of HD 209458b's radiative zone, which has a horizontal to vertical aspect ratio of ~100. Analysis of the terms in the full Navier-Stokes vertical momentum equation reveals that, even in the supersonic flow regime obtained here, the vertical acceleration and curvature terms would have magnitudes only ~1% and ~10% that of the hydrostatic terms at the photosphere and top of the model, respectively. The caveat to this result is that vertical accelerations can still be important for subgrid scale structures. These simulations also do not include the possible effects of vertically propagating shocks, which can conceivably dissipate atmospheric kinetic energy.

To confirm the effects shown in Figure 1, we have run additional simulations using one-dimensional radiative-equilibrium temperature profiles from Burrows et al. (2003) and Chabrier et al. (2004), which are significantly hotter than that of Iro et al. (2005) due to differing assumptions about the heat redistribution. We have also experimented with changing the value of the free parameter ΔT_{eq}, which controls the strength of the radiative forcing in our Newtonian cooling scheme (eq. [1]). We have run simulations at ΔT_{eq} of 100, 250, 500, 750, and 1000 K. The essential features of the simulation presented here are representative of the results of the other simulations performed: they all develop a stable superrotating jet at the equator extending to the midlatitudes and a hot region of atmosphere downwind of the substellar point. But for a given ΔT_{eq}, the simulated temperature *differences* are not affected by which group's radiative-equilibrium temperature profile is used. For values of ΔT_{eq} between 500 and 1000 K, the simulations all produce temperature contrasts at the photosphere ranging from 300 to 600 K, with peak equatorial wind speeds in the range 2–5 km s^{-1}. The simulations employing the atmospheric profiles of Burrows et al. (2003) and Chabrier et al. (2004) do, however, produce hotter (by ~500 K) mean photospheric temperatures than our nominal case.

We have also run the model with a different initial condition. We started this alternate simulation with identical input parameters to the simulation shown in Figure 1 but with a retrograde zonal wind profile: $u = -3 \text{ km s}^{-1} \cos^4 \phi \tan^{-1}(2 \text{ bar}/p)$. We set the meridional wind v to zero and set the pressures to be in gradient-wind balance with the initial winds (Holton 1992). After 5000 days of integration time, a strong superrotating jet at the equator at 220 mbar develops in the simulation, with maximum wind speeds of 3.4 km s^{-1} and temperature contrasts of ~430 K. The similarity with the simulation presented in Figure 1 shows that the overall flow geometry is not strongly sensitive to the initial conditions.

Our results differ from the one-layer shallow-water simulations of Cho et al. (2003), who find that the mean-equatorial flow for HD 209458b is westward. Shallow-water turbulence simulations consistently produce westward equatorial flow, even for planets such as Jupiter and Saturn whose equatorial jets are eastward (Cho & Polvani 1996; Iacono et al. 1999a, 1999b; Peltier & Stuhne 2002; Showman 2004). This effect may result from the exclusion of three-dimensional momentum-transport processes in one-layer models. For example, three-dimensional effects are important in allowing equatorial superrotation in numerical models of Venus, Earth, and Jupiter (Del Genio & Zhou 1996; Saravanan 1993; Williams 2003). Nevertheless, the shallow-water turbulence models successfully capture essential aspects of midlatitude jets for giant planets in our solar system (Cho & Polvani 1996).

4. ORBITAL PHASES AND PREDICTED LIGHT CURVE

To illustrate the observable effects of the circulation, Figure 2 shows orthographic projections (Snyder 1987) of the black-

body flux of HD 209458b on the 220 mbar level. The key feature is the hot region downstream from the substellar point, which faces Earth after the transit and before the secondary eclipse. This pattern differs drastically from that expected in the absence of winds, in which case the hottest regions would be at the substellar point.

We show the IR light curve of the planet as predicted by our simulations in Figure 3. The circles represent the total flux received at Earth from the planet every 10° in its orbit. The points are derived by integration of the radiation intensity emitted into a solid angle projected in the direction toward Earth. We assume in this calculation that each column of the atmosphere at the photosphere emits radiation with the intensity of a blackbody, $\sigma T^4/\pi$, with temperatures varying as shown in Figure 1*b*. We use 223 mbar for the photospheric pressure, which is the layer closest to where the effective temperature in the Iro et al. (2005) model equals their computed actual temperature.

The model predicts a phase lead of 60°—or 14 hr—between peak radiation from the planet and the secondary eclipse, when the illuminated hemisphere faces Earth. Using the ~500 K temperature contrasts shown in Figure 3, we derive a ratio of 2.2 between the maximum and minimum flux. To confirm the validity of this prediction, we performed analogous light-curve calculations assuming the IR flux is emitted from a single pressure level ranging from 150 to 450 mbar, where the photosphere conceivably could be. The magnitude of the flux ratio ranges from 3.2 to 1.4 over this range of pressures. Our predicted phase lead of 60° shifts by $\pm 20°$ over this range of pressures. These effects are inversely correlated: if the photosphere pressure is less than 220 mbar, then the flux ratio increases but the phase shift decreases and vice versa.

Nevertheless, the possible formation of clouds high in the atmosphere of HD 209458b ($p < 200$ mbar)—which we have not treated here—may significantly alter the radiation budget.

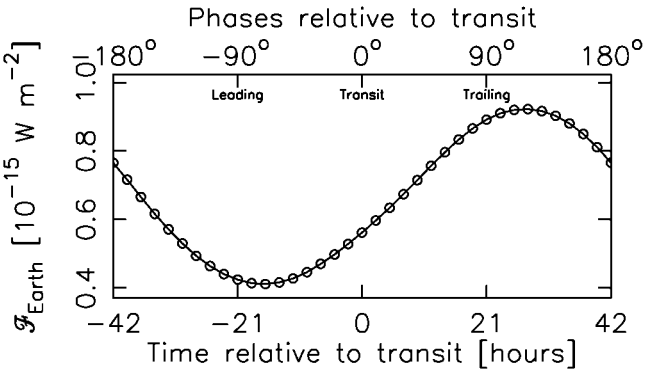

FIG. 3.—Synthetic light curve of the 220 mbar layer of our model atmosphere for HD 209458b. This simulation predicts peak emission from the planet 14 hr *before* the time of the secondary eclipse.

In addition, uncertainties in the input parameters and the Newtonian cooling approximation limit the precision with which we can predict the magnitude of the effects described above. A major future advance in the characterization of close-in EGP atmospheres will come from coupling dynamics and radiative transfer directly. We note, however, that the inputs to such a model are likely to be somewhat hypothetical as well, given the limited constraints available from observations.

Special thanks to T. Guillot, N. Iro, and B. Bézard for valuable guidance on the radiative time constant prior to publication of their results. Thanks also to the referee, J. W. Barnes, J. J. Fortney, P. J. Gierasch, and many others for advice on the project and manuscript. Figures were created using the free Python Numarray and PLplot libraries. This research was supported by NSF grant AST-0307664 and NASA GSRP NGT5-50462.

REFERENCES

Anders, E., & Grevesse, N. 1989, Geochim. Cosmochim. Acta, 53, 197
Brown, T. M., Charbonneau, D., Gilliland, R. L., Noyes, R. W., & Burrows, A. 2001, ApJ, 552, 699
Burrows, A., Hubeny, I., Hubbard, W. B., Sudarsky, D., & Fortney, J. J. 2004, ApJ, 610, L53
Burrows, A., Sudarsky, D., & Hubbard, W. B. 2003, ApJ, 594, 545
Chabrier, G., Barman, T., Baraffe, I., Allard, F., & Hauschildt, P. H. 2004, ApJ, 603, L53
Charbonneau, D., Brown, T. M., Latham, D. W., & Mayor, M. 2000, ApJ, 529, L45
Charbonneau, D., Brown, T. M., Noyes, R. W., & Gilliland, R. L. 2002, ApJ, 568, 377
Charbonneau, D., et al. 2005, ApJ, 626, 523
Cho, J. Y.-K., Menou, K., Hansen, B. M. S., & Seager, S. 2003, ApJ, 587, L117
Cho, J. Y.-K., & Polvani, L. M. 1996, Science, 273, 335
Cooper, C. S., Sudarsky, D., Milsom, J. A., Lunine, J. I., & Burrows, A. 2003, ApJ, 586, 1320
Del Genio, A. D., & Zhou, W. 1996, Icarus, 120, 332
Deming, D., Seager, S., Richardson, L., & Harrington, J. 2005, Nature, 434, 740
Fortney, J. J., Sudarsky, D., Hubeny, I., Cooper, C. S., Hubbard, W. B., Burrows, A., & Lunine, J. I. 2003, ApJ, 589, 615
Goukenleuque, C., Bézard, B., Joguet, B., Lellouch, E., & Freedman, R. 2000, Icarus, 143, 308
Guillot, T., Burrows, A., Hubbard, W. B., Lunine, J. I., & Saumon, D. 1996, ApJ, 459, L35
Henry, G. W., Marcy, G. W., Butler, R. P., & Vogt, S. S. 2000, ApJ, 529, L41
Holton, J. R. 1992, An Introduction to Dynamic Meteorology (3rd ed.; New York: Academic)
Iacono, R., Struglia, M. V., & Ronchi, C. 1999a, Phys. Fluids, 11, 1272
Iacono, R., Struglia, M. V., Ronchi, C., & Nicastro, S. 1999b, Nuovo Cimento C, 22, 813
Iro, N., Bézard, B., & Guillot, T. 2005, A&A, 436, 719
Kalnay, E. 2003, Atmospheric Modeling, Data Assimilation and Predictability (Cambridge: Cambridge Univ. Press)
Laughlin, G., Wolf, A., Vanmunster, T., Bodenheimer, P., Fischer, D., Marcy, G., Butler, P., & Vogt, S. 2005, ApJ, 621, 1072
Limaye, S. S., & Sromovsky, L. A. 1991, J. Geophys. Res., 96, 18941
Peltier, W. R., & Stuhne, G. R. 2002, in Meteorology at the Millennium, ed. R. P. Pearce (New York: Academic), 43
Saravanan, R. 1993, J. Atmos. Sci., 50, 1211
Showman, A. P. 2004, BAAS, 36, 1135
Showman, A. P., & Guillot, T. 2002, A&A, 385, 166
Snyder, J. P. 1987, Map Projections—A Working Manual (US Geological Survey Professional Paper 1395; Washington, DC: US Government Printing Office)
Suarez, M. J., & Takacs, L. L. 1995, Documentation of the AIRES/GEOS Dynamical Core, ver. 2 (NASA Tech. Memo 104606, Vol. 5; Greenbelt: GSFC)
Vidal-Madjar, A., Lecavelier des Etangs, A., Désert, J.-M., Ballester, G. E., Ferlet, R., Hébrard, G., & Mayor, M. 2003, Nature, 422, 143
Vidal-Madjar, A., et al. 2004, ApJ, 604, L69
Williams, G. P. 2003, J. Atmos. Sci., 60, 1270